The G0 experiment

C. Furget

THE G^0 EXPERIMENT *

C. FURGET FOR THE G^0 COLLABORATION

Institut des Sciences Nucléaires,
53 avenue des Martyrs,
38026 GRENOBLE Cedex, FRANCE
E-mail: furget@isn.in2p3.fr

The G^0 experiment is dedicated to the determination of the strange quarks contribution to the electric and magnetic nucleon form factors for a large range of momentum transfers between 0.1 to 1 $(GeV/c)^2$. These information will be provided by the asymmetries of cross-sections measured with longitudinaly polarized electrons in the elastic electron-proton scattering and quasi-elastic electron-deuteron scattering. A set of measurements at three different Q^2 will allow the complete separation of the electric and magnetic weak, as well as axial nucleon form factors. This report summarizes the physics case and gives details about the dedicated set-up which will be used. The experiment, which will be performed at *Jefferson Laboratory*, should start at the end of 2002 for the forward angle and should be achieved after backward angle measurements in 2006.

1. Introduction

In Quantum Chromodynamics, the nucleon is viewed as composed of three valence u and d quarks and a sea of gluons and quark-antiquark pairs ($u\bar{u}$, $d\bar{d}$, $s\bar{s}$ ...). Because the strange quarks contribute only to the sea, their contribution to the nucleon properties is one of the open questions which is investigated in a joint experimental and theoretical study.

Deep inelastic neutrino scattering experiments provide indication that strange quarks contribute to a large fraction of the momentum carried by the sea quarks [1]. However no conclusive information exist on the difference between s and $\bar{s}$ distributions. Other measurements of spin dependent structure functions in deep inelastic scattering indicates that $s\bar{s}$ pairs could have a relatively large influence (up to 30%) to the nucleon spin structure [2,3] but with still large theoretical and experimental uncertainties. At low energy the sigma term obtained from π-nucleon scattering indicates a contribution of strangeness of about 130 MeV to the nucleon mass but with some large uncertainties in the analysis [4].

*to be published in the proceedings of the pavi2002 conference

The parity-violating (PV) electro-weak interaction in the electron-nucleon elastic scattering appears to offer a unique opportunity to study the electro-weak nucleon structure [5,6,7]. The measurement of the neutral weak nucleon form factors provides another determination of the contribution of strange quarks to the electric and magnetic properties of the nucleon [8,9], and in particular possible difference in the s and $\bar{s}$ spatial densities. The PV asymmetry allows also to measure the axial form factor in electron elastic scattering, which can be compared to those accessible from neutrino elastic scattering [12], and which provides new information on the influence of the axial coupling of the photon to the nucleon in the anapole form factor.

Several dedicated PV asymmetry experiments and apparatus have been developped during the last decade for these studies [9,10,11]. In this contribution we focus on the G^0 experiment which should provide the most complete determination of the contribution of the strange quarks to the electric, magnetic and axial form factors. Besides a complete separation of these three form factors, data will be obtained over a large range of momentum transfers (Q^2 between 0.1 to 1 $(GeV/c)^2$). Thanks to the large acceptance of the set-up, the G^0 experiment will also provide information on the weak neutral transition current in the Δ resonance. This last topic is explained in details in another contribution to these proceedings [13].

The formalism used in parity-violating experiments is developped in section 2. The section 3 focuses on the G^0 experiment with its expected results and errors associated to the strange form factors. The experimental set-up is described in section 4 with two different parts related to the forward and backward angles corresponding to two different kinematical ranges which will be explored.

2. Elastic scattering and parity violating experiment

2.1. *The electroweak nucleon form factors*

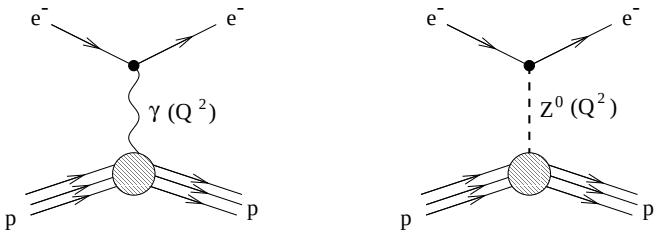

Figure 1. Electroweak interaction in electron-nucleon scattering

In the electron-nucleon scattering, the electroweak interaction takes place at first

order through two diagrams, one corresponding to the exchange of a virtual photon and one to the exchange of a Z^0 with a 4-momentum transferred $-Q^2 = \nu^2 - \vec{q}^{\,2} = -4E_e E'_e \sin^2\left(\frac{\theta_e}{2}\right)$, where E_e is the energy of the incident electron which is scattered at an angle θ_e with an energy E'_e. The momentum $\vec{q}$ is related to the characteristic distance probed in the nucleon with $\mid \vec{q} \mid \sim 1/\mathrm{r}$. Typically for momentum transfers of the order of 1 (GeV/c), the spatial resolution is much better than the nucleon size.

The scattering amplitudes, corresponding to the exchange of a virtual photon for $\mathcal{M}_\gamma$ and to the exchange of a Z^0 for $\mathcal{M}_Z$ are expressed in terms of the leptonic and hadronic currents through the relations :

$$\mathcal{M}_\gamma = (ie)^2 \langle e'|\gamma_\mu|e\rangle \left(\frac{-ig^{\mu\nu}}{q^2}\right) \langle P'|\hat{\mathcal{J}}_\nu^{(\gamma,p)}|P\rangle \tag{1}$$

$$\mathcal{M}_Z = \left(\frac{ig}{cos\theta_W}\right)^2 \langle e'|\gamma^\mu (C_V^e - \gamma^5 C_A^e)|e\rangle \left(\frac{-i\left(g^{\mu\nu} - \frac{q^\mu q^\nu}{M_Z^2}\right)}{q^2 - M_Z^2}\right) \langle P'|\hat{\mathcal{J}}_\nu^{(Z,p)}|P\rangle$$

where C_V^e and C_A^e are respectively the vector and vector-axial coupling of the electron (see table 1).

Table 1. *Electric charge, third component of the weak isospin, vector coupling* $C_V^f = 2T_3^f - 4Q_f \sin^2\theta_W$ *and vector-axial coupling* $C_A^f = -2T_3^f$ *of charged particles.*

Fermions			Q_f	T_3^f	C_A^f	C_V^f
$\begin{pmatrix}\nu_e\\ e\end{pmatrix}$	$\begin{pmatrix}\nu_\mu\\ \mu\end{pmatrix}$	$\begin{pmatrix}\nu_\tau\\ \tau\end{pmatrix}$	0	$\frac{1}{2}$	-1	1
			-1	$-\frac{1}{2}$	1	$-1 + 4\sin^2\theta_W$
$\begin{pmatrix}u\\ d\end{pmatrix}$	$\begin{pmatrix}c\\ s\end{pmatrix}$	$\begin{pmatrix}t\\ b\end{pmatrix}$	$\frac{2}{3}$	$\frac{1}{2}$	-1	$1 - \frac{8}{3}\sin^2\theta_W$
			$-\frac{1}{3}$	$-\frac{1}{2}$	1	$-1 + \frac{4}{3}\sin^2\theta_W$

The elastic scattering is then described by the coherent sum of the amplitudes $\mathcal{M}_\gamma$ and $\mathcal{M}_Z$ with the expression of the cross-section given by :

$$\frac{d\sigma}{d\Omega} \propto |\mathcal{M}|^2 = |\mathcal{M}_\gamma + \mathcal{M}_Z|^2 \tag{2}$$

For momentum transfers Q^2 of the order of 1 GeV, $\mathcal{M}_Z$ is about 10^4 times smaller than $\mathcal{M}_\gamma$. Because of normalization factors (target, solid angle ...), cross-section measurements do not allow to extract $\mathcal{M}_Z$ with the required precision of a few %.

By neglecting the weak amplitude, we can derive the usual expression for the cross-section of the elastic electron-nucleon scattering given by :

$$\frac{d\sigma}{d\Omega} = \frac{d\sigma}{d\Omega}_{Mott} \left[\frac{{G_E^{(\gamma,p)}}^2(Q^2) + \tau {G_M^{(\gamma,p)}}^2(Q^2)}{(1+\tau)} + 2\tau \tan^2\left(\frac{\theta_e}{2}\right) {G_M^{(\gamma,p)}}^2(Q^2)\right] \tag{3}$$

with $\tau = \frac{Q^2}{4M^2}$. The Mott cross-section $\left(\frac{d\sigma}{d\Omega}\right)_{Mott}$ corresponds to the scattering of electrons from a pointlike nucleon without spin. $G_E^{(\gamma,p)}$ et $G_M^{(\gamma,p)}$ are the Coulomb (also called electric) and magnetic proton form factors, which come from the multipole expansion of the hadronic current on the total angular momentum of the virtual photon [14]. These two form factors, which are related to the electromagnetic finite spatial distributions of the nucleon, can be interpreted in the Breit frame as the Fourier transform of the charge and magnetic moment densities inside the nucleon. They are related to the static properties of the proton at $Q^2 = 0$ ($G_E(0) = 1$ and $G_M(0) = \mu_p = 2.793\,\mu_N$).

Experimentally, a Rosenbluth separation of these two form factors is possible by varying the energy E_e of the incident electron or the scattering angle θ_e to perform different measurements at fixed Q^2 (τ is fixed also).

Because the weak interaction does not conserve parity, $\mathcal{M}_Z$ can be accessible through the asymmetry measurement of the cross-sections associated to elastic scattering of longitudinaly polarized electrons with two opposite helicities :

$$A_{PV} = \frac{|\mathcal{M}^+|^2 - |\mathcal{M}^-|^2}{|\mathcal{M}^+|^2 + |\mathcal{M}^-|^2} \simeq \frac{\mathcal{R}e(\mathcal{M}_\gamma \mathcal{M}_Z^*)^+ - \mathcal{R}e(\mathcal{M}_\gamma \mathcal{M}_Z^*)^-}{2|\mathcal{M}_\gamma|^2} \tag{4}$$

Asymmetry as small as few 10^{-6} can be extracted with few % of precision thanks to cancellation of normalization systematic errors in the ratio of the cross-section measurements. In the elastic electron-nucleon scattering, the multipole expansion of the electro-weak charge and currents introduce, in the expression of the asymmetry, three additionnal weak form factors : the vector Coulomb $G_E^{(Z,p)}$, vector magnetic $G_M^{(Z,p)}$ and axial G_A^{ep} form factors. The asymmetry is then rewritten as :

$$A_{PV}^p = -\left(\frac{G_F Q^2}{4\sqrt{2}\pi\alpha}\right) \frac{\epsilon\, G_E^{(\gamma,p)} G_E^{(Z,p)} + \tau\, G_M^{(\gamma,p)} G_M^{(Z,p)} - (1 - 4sin^2\theta_W)\epsilon'\, G_M^{(\gamma,p)} G_A^{ep}}{\epsilon \left(G_E^{(\gamma,p)}\right)^2 + \tau \left(G_M^{(\gamma,p)}\right)^2} \tag{5}$$

where τ is already defined and,

$$\begin{aligned} \epsilon &= \frac{1}{1 + 2(1+\tau)tan^2\frac{\theta_e}{2}} \\ \epsilon' &= \sqrt{\tau(1+\tau)(1-\epsilon^2)} \end{aligned} \tag{6}$$

Three independent measurements are required for a complete determination of the three form factors $G_E^{(Z,p)}$, $G_M^{(Z,p)}$ and G_A^{ep}. This could be performed by varying the kinematical factors (ϵ and ϵ') at a fixed Q^2. Forward and backward (scattered electron) angles measurements correspond respectively to small ϵ (large ϵ') and large ϵ (small ϵ'). As a third measurement, it appears more effective [15] to measure the

asymmetry in quasi-elastic scattering on the deuterium, which implies the proton and the neutron. In the impulse approximation the asymmetry can be written :

$$A_{QE} = \frac{\sigma_p A_p + \sigma_n A_n}{\sigma_{QE}} \tag{7}$$

where the asymmetry on the proton A_p is given by relation 5 and the one on the neutron A_n is expressed as :

$$A_n = -\left(\frac{G_F Q^2}{4\sqrt{2}\pi\alpha}\right) \frac{\epsilon\, G_E^{(\gamma,n)} G_E^{(Z,n)} + \tau\, G_M^{(\gamma,n)} G_M^{(Z,n)} - (1-4sin^2\theta_W)\epsilon'\, G_M^{(\gamma,n)} G_A^{en}}{\epsilon \left(G_E^{(\gamma,n)}\right)^2 + \tau \left(G_M^{(\gamma,n)}\right)^2} \tag{8}$$

For reliable calculation the simple form of equation 7 has to be corrected from final state interaction and other nuclear corrections [16,17].

2.2. *Strange form factors*

As already mentionned, the parity violating experiments can provide information related to the strange quarks of the sea. For this purpose the hadronic currents can be rewritten separately for the electromagnetic and weak parts as :

$$\begin{aligned} \mathcal{J}_\mu^{(\gamma,N)} &= \sum_{q=u,d,s} Q_q \mathcal{J}_V^{(\gamma,q)} \\ \mathcal{J}_\mu^{(Z,N)} &= \sum_{q=u,d,s} \left[C_V^q \mathcal{J}_\mu^{(Z,q)} + C_A^q \mathcal{J}_\mu^{(Z,q)}\right] \end{aligned} \tag{9}$$

where C_V^q et C_A^q are respectively the vector and axial coupling of the quark of flavour q given in table 1. The approximation, which consist by neglecting the three heavy flavours, is valid because of their larger mass.

The decomposition can directly be expressed on the form factors as :

$$\begin{aligned} G_{E,M}^{(\gamma,N)} &= \sum_{q=u,d,s} Q_q G_{E,M}^{(q,N)} \\ G_{E,M}^{(Z,N)} &= \sum_{q=u,d,s} C_V^q G_{E,M}^{(q,N)} \\ G_A^{eN} &= \sum_{q=u,d,s} C_A^q G_A^{(q,N)} \end{aligned} \tag{10}$$

When applying these relations to the proton and neutron, the number of form factors for the three quark flavours u, d and s becomes equal to 18. A second approximation is made using the charge symmetry under the exchange of u and d quarks ($G_{E,M}^{(u,p)} = G_{E,M}^{(d,n)}$) and s quark ($G_{E,M}^{(s,p)} = G_{E,M}^{(s,n)}$). It is then possible to express the electric and magnetic quark form factors (vector currents) as a function

of electromagnetic and weak form factors of the proton and neutron :

$$G^u_{E,M} = \left(3 - 4sin^2\theta_W\right) G^{(\gamma,p)}_{E,M} - G^{(Z,p)}_{E,M} \tag{11}$$

$$G^d_{E,M} = \left(2 - 4sin^2\theta_W\right) G^{(\gamma,p)}_{E,M} + G^{(\gamma,n)}_{E,M} - G^{(Z,p)}_{E,M} \tag{12}$$

$$G^s_{E,M} = \left(1 - 4sin^2\theta_W\right) G^{(\gamma,p)}_{E,M} - G^{(\gamma,n)}_{E,M} - G^{(Z,p)}_{E,M} \tag{13}$$

The contribution of the strange quarks to the electric and magnetic nucleon form factors can then directly be extracted from the measurement of $G_E^{(Z,p)}$ and $G_M^{(Z,p)}$. The other four nucleon electromagnetic form factors being obtained from other experiments, uncertainties associated to $G_E^{(\gamma,n)}$ have to be considered in the extraction.

The asymmetry, given by relation 5, can be decomposed into two terms :

$$A_{PV} = A^0_{PV} + A^s_{PV} \tag{14}$$

the first one beeing independent of the strange form factors :

$$A^0_{PV} = -\left(\frac{G_F Q^2}{4\sqrt{2}\pi\alpha}\right) \frac{1}{\epsilon \left(G_E^{(\gamma,p)}\right)^2 + \tau \left(G_M^{(\gamma,p)}\right)^2} \left[\epsilon\, G_E^{(\gamma,p)} \left((1 - 4sin^2\theta_W) G_E^{(\gamma,p)} - G_E^{(\gamma,n)}\right)\right.$$
$$\left. + \tau\, G_M^{(\gamma,p)} \left((1 - 4sin^2\theta_W)\, G_M^{(\gamma,p)} - G_M^{(\gamma,n)}\right) - (1 - 4sin^2\theta_W)\epsilon' G_M^{(\gamma,p)} G_A^{ep}\right] \tag{15}$$

and the second term involving the contribution of G_E^s et G_M^s :

$$A^s_{PV} = \left(\frac{G_F Q^2}{4\sqrt{2}\pi\alpha}\right) \frac{G_E^{(\gamma,p)} G_E^s + \tau\, G_M^{(\gamma,p)} G_M^s}{\epsilon \left(G_E^{(\gamma,p)}\right)^2 + \tau \left(G_M^{(\gamma,p)}\right)^2} \tag{16}$$

This expression shows that the asymmetry is already non zero even if the strange quarks do not contribute to the nucleon properties.

2.3. *Theoretical predictions on G_E^s et G_M^s*

Some complete and recent reviews [9,10,11] have been devoted on the subject and are discussed in several contributions of these proceedings.

A class of models [18,19] introduce the strange quarks contribution as loops containing kaons and hyperons in the nucleon structure. In other models [20,21], the strangeness appears through the coupling of the virtual photon to the ϕ (VDM model). Now Lattice QCD calculations become available but with large uncertainties [22]. Other models are based on chiral symmetry [23] or dispersion relations [24].

The comparison between the predictions of these models is generally performed on the contribution of strange quarks to the static nucleon properties, given by the strangeness magnetic moment $\mu_s = G_M^s(Q^2 = 0)$ and the strangeness charge radius r_s^2 = -6 $\left[G_E^s/dQ^2\right]_{Q^2=0}$, i.e. at zero Q^2. Most models predict negative values

for μ_s between -0.8 and 0, often around -0.3, which corresponds to about 10% of the proton magnetic moment. The predicted values for r_s^2 are often small, without agreement about the sign of r_s. A maximum value of about 0.005 fm^2 for r_s^2 has been derived from neutrino deep inelastic scattering [25]. Right now almost nothing is known about the Q^2 dependence, which will be explored by the G^0 experiment between 0.1 to 1 GeV^2.

2.4. *The axial form factor* G_A^{ep}

The axial form factor G_A^{eN} has been considered for a long time as a quantity to be predicted for the extraction of G_E^s et G_M^s (see relation 15). It appears now that it contains information, with theoretical and experimental implication in atomic parity violation [12]. It can be expressed through the relation :

$$G_A^{eN}(Q^2) = G_A^{Z,N}(Q^2) + \eta F_A(Q^2) + R_e \tag{17}$$

The first term $G_A^Z = -\tau_3 G_A + G_A^s$ corresponds to the weak axial form factor associated to the Z^0 exchange (graph a/ of figure 2). It is measured at $Q^2 = 0$ in neutron beta decay ($G_A(0)$=1.2601 $\pm$ 0.0025) and its Q^2 dependence is measured in charged current neutrino experiment [26]. The strange spin fraction $G_A^s(Q^2)$ is measured at Q^2=0 in deep inelastic scattering [3].

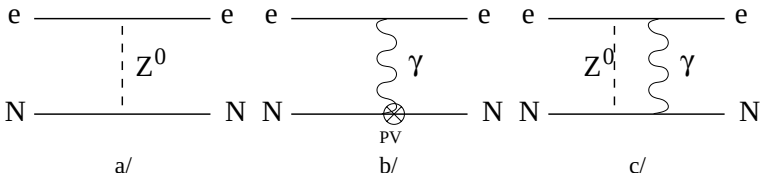

Figure 2. Various contributions to the axial form factor G_A^{eN}

The second term corresponds to the nucleon anapole form factor, which involves vector coupling at the electron vertex and axial coupling at the nucleon vertex (as graph b/ of figure 2). This term is dominated at first order by the $\gamma - Z$ mixing amplitude and has a relative contribution, which is enhanced by the factor $\eta = \frac{8\pi\sqrt{2}\alpha}{1-4sin^2\theta_W} \simeq 3.45$ (see relation 17). The third term is related to other electroweak radiative corrections (as graph c/ of figure 2).

It has to be stressed that very few theoretical calculations exist for the anapole term and the electroweak radiative corrections. A large uncertainty is given by reference [27] on the calculation of $F_A(0) = 0.03 \pm 0.24$ and reference [28] has found a Q^2 dependence for F_A very different from the dipole form usually used in the predictions.

2.5. *The other experiments*

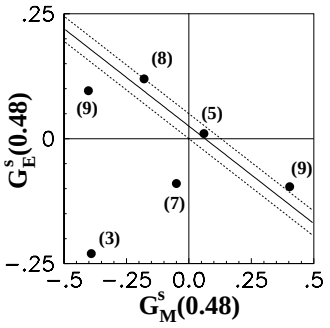

Figure 3. HAPPEX result from reference [29]. Points refer to different models.

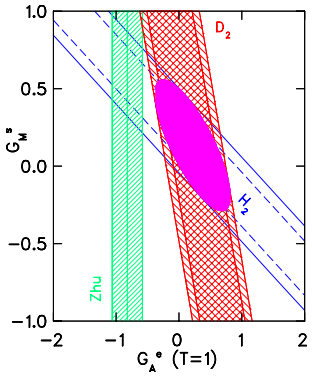

Figure 4. SAMPLE result from references [30,31] with theoretical prediction of G_A^{eN} from Zhu [27].

Because the contribution of the strange form factors is of great interest for the hadronic community, several experiments have been proposed on the subject. Some have already been completed and preliminary conclusions can be derived.

The *HAPPEX* experiment [29], which was performed in the hall A of *Jefferson Laboratory*, has measured the asymmetry on the proton at $Q^2 = 0.477\,(GeV/c)^2$ for forward scattering angles of the electron. It has allowed the extraction of a linear combination $G_E^s + 0.392 G_M^s$, which was found compatible with zero. However, the result, plotted on figure 3, does not provide separate contribution of the strange quarks from the two form factors.

The *SAMPLE* experiment, which was performed at Bates, has measured asymmetries on proton and deuteron for backward scattering angles for $Q^2 = 0.1(GeV/c)^2$ [30,31]. These measurements allowed the separation of the magnetic G_M^s and axial G_A^e form factors. The results, reported in figure 4, have shown a disagrement with theoretical expectation on G_A^e. A new measurement at $Q^2 = 0.04\,(GeV/c)^2$ has been performed in order to confirm (or not) the observed discrepancy [15,32].

The experiment *PVA4*, which is performed at the MAMI facility, has measured asymmetry on the proton at scattering angles of 30 to 40° for $Q^2 = 0.2\,(GeV/c)^2$, and is sensitive to the combinaison $G_E^s + 0.22 G_M^s + 0.04 G_A^e$ [33].

A second asymmetry measurement on the proton at small scattering angle 6° and $Q^2 = 0.1\,(GeV/c)^2$ will be performed by the *HAPPEX* collaboration in 2003 [34]. This measurement, combined with *SAMPLE* results should allow the complete separation of the three form factors. Also the collaboration will measure the asym-

metry on the ^4He nucleus, which is only sensitive to the electric form factor G_E^s.

As shown previously, existing data provide little constraints on theoretical predictions. A complete separation of the three electric, magnetic and axial form-factors at various momentum transfers is needed to remove ambiguities on the interpretation of the results.

3. The G^0 experiment

The G^0 collaboration proposes to perform the separation of the electric G_E^s, magnetic G_M^s and axial G_A^{ep} form factors for three different momentum tranfers 0.3, 0.5 and 0.8 $(GeV/c)^2$.

A first asymmetry measurement will be performed for forward electron scattering angles between 7 and 15° for a large Q^2 range between 0.1 and 1 $(GeV/c)^2$. This measurement is obtained in a single run by detecting the recoil protons at a fixed angle between 68 and 78° from the elastic electron-proton scattering. This measurement corresponds to values for the polarisation ϵ close to 1. The second measurement will be performed at backward electron scattering angle of about 108° for the hydrogen and deuterium targets. Here the Q^2 acceptance is limited and three separate measurements are planned for different incident beam energies of 424, 525 and 799 MeV, corresponding to Q^2 of 0.3, 0.5 and 0.8 $(GeV/c)^2$ with a fixed scattered electron angle centered at 110°. Measurement on the hydrogen corresponds to ϵ values of about 0.2 in relation 8, whereas measurement on the deuterium involves also the contribution on the neutron with different values for the electromagnetic form factors in relation 8.

Table 2. Different kinematics proposed for the G^0 experiment. In column "measurement", A_{forw} and A_{back} indicate the forward and backward modes on hydrogen target and A_{deut} the backward measurement on deuterium.

$Q^2(GeVc)^2$	Measurement	$\theta(deg)$	$E_e(GeV)$	η	ξ	χ	ψ
0.3	A_{forw}	11	3.	-7.7	32.6	7.9	0.4
0.3	A_{back}	110	0.424	-15.9	11.9	15.3	4.0
0.3	A_{deut}	110	0.424	-22.2	9.6	3.5	5.0
0.5	A_F (LH_2)	13	3.	-16.7	60.8	25.0	1.4
0.5	A_B (LH_2)	110	0.585	-29.0	18.0	40.3	8.5
0.5	A_B (LD_2)	110	0.585	-39.8	14.7	9.0	10.1
0.8	A_F (LH_2)	16	3.	-32.9	112.7	76.2	4.6
0.8	A_B (LH_2)	110	0.799	-49.3	28.0	106.5	18.4
0.8	A_B (LD_2)	110	0.799	-66.7	23.3	23.4	21.6

These forward and backward (on hydrogen and deuterium targets) asymmetry

measurements can be expressed as :

$$A_{PV} = \eta + \xi G_E^s + \chi G_M^s + \psi G_A^e \, (T = 1) \tag{18}$$

where η , ξ , χ and ψ , which include kinematical factors and the electromagnetic form factors, are listed on table 2 for the three $Q^2 = 0.3$, 0.5 and 0.8 $(GeV/c)^2$. It demonstrates how each measurement maximizes the contribution of one form factor, allowing a good separation of G_E^s, magnetic G_M^s and axial G_A^{ep}.

Table 3. Relative contribution of experimental (both statistical and systematic) errors on the G_E^s, G_M^s and G_A^e uncertainties (see text).

	G_E^s			G_M^s			$G_A^e(T=1)$		
Q^2 $(GeV/c)^2$	0.30	0.50	0.80	0.30	0.50	0.80	0.30	0.50	0.80
A_{forw} (%)	20.3	11.4	12.5	0.2	0.1	0.1	1.5	0.7	0.7
A_{back} (%)	31.0	34.3	37.8	50.3	47.4	47.9	0.9	0.8	0.9
A_{deut} (%)	14.3	17.1	22.0	23.3	23.7	27.9	61.8	62.6	72.6
G_E^p (%)	2.1	1.9	1.0	0.0	0.0	0.0	1.1	0.4	0.1
G_M^p (%)	1.5	1.3	0.6	0.9	1.2	1.0	0.4	0.8	0.8
G_E^n (%)	12.2	10.9	5.7	0.3	0.2	0.1	0.9	0.6	0.3
G_M^n (%)	0.9	0.9	0.6	1.4	2.0	1.9	3.8	3.1	1.9
Q^2 (%)	4.4	4.9	3.7	5.0	4.8	3.3	7.2	6.9	4.8
P_e (%)	11.4	14.3	11.8	15.6	16.5	12.5	22.3	23.8	17.8
$G_A^e(T=0)$ (%)	1.8	3.1	4.2	3.0	4.2	5.3	0.1	0.2	0.2

Statistical and systematic errors have been calculated for the G^0 experiment on the three form factors G_E^s, G_M^s and G_A^{ep} $(T = 1)$ at $Q^2 = 0.3$, 0.5 and 0.8 $(GeV/c)^2$ after extraction from the asymmetries (see relation 18). These results have been reported on table 3. This calculation has been obtained with a data taking of 700 h in the forward angle mode whereas 700 h are required for each backward angle asymmetry measurement both on hydrogen and deuterium targets. It is assumed also a 70 $\pm$ 2 % of polarisation of the longitudinaly polarized electrons beam with an intensity of 40 μA. Other errors, which have been reported are coming from the electromagnetic form factors, with a 20 % uncertainty for G_E^n. Also theoretical uncertainty has to be included on the isocalar part of the axial form factor which is not accessible from asymmetry measurement. The last contribution to the error is coming from determination of the momentum tranfers Q^2 which will be measured at the 1 % level. From table 3, it can be seen that the main contribution to the errors comes from the statistical ones associated to the three independent measurements (forward and backward hydrogen and deuterium). They will contribute at the same level to the G_E^s error whereas only the statistical error associated to the backward deuterium asymmetry will contribute to the determination of G_A^{ep} $(T = 1)$. In all cases the systematic errors will be dominated by the polarization measurement and a good precision on Q^2 determination is important to reduce the associated systematic

error. Finally the main contribution for the electromagnetic form factors is coming from G_E^n and is affecting the determination of G_E^s.

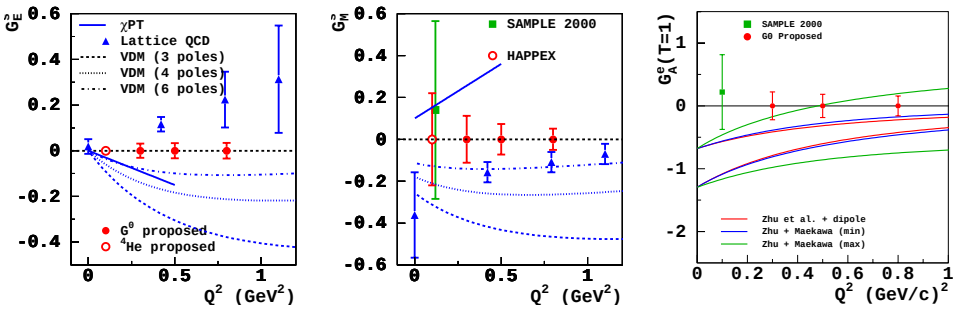

Figure 5. Expected errors associated to the G^0 experiment for the three form factors G_E^s, G_M^s and G_A^e. Results from $SAMPLE$ experiment as well as expected errors from $HAPPEX2$ (on hydrogen and helium targets) are also reported.

To complete this discussion on errors, figures 5 show the expected errors on G_E^s, G_M^s and G_A^{ep} from G^0 measurements. They are compared to past and future experiments (see section 2.5), and with some theoretical calculations (see section 2.3). The $HAPPEX$ result is not shown because the separation of G_E^s and G_M^s was not possible from their asymmetry measurement. It can be seen that no agreement exists on the sign of G_E^s and strong differences exist on the Q^2 dependence predicted by various models. In this context $HAPPEX2$ will provide strong constraint at small Q^2 useful for the extraction of the strangeness charge radius whereas G^0 will provide information constraining the Q^2 dependence of G_E^s. For G_M^s, $HAPPEX2$ will improve the existing data provided by $SAMPLE$ at small Q^2 whereas G^0 experiment will cover again larger Q^2 range where models disagree strongly. As already mentionned very few theoretical predictions exist for the isovector part of the axial form factor both at $Q^2 = 0$ and on the Q^2 dependence which could differ strongly from the usual dipole form. The result obtained by $SAMPLE$ collaboration differs in sign from theoretical expectation and a second measurement will be available at smaller Q^2 [15,32]. Again G^0 results are expecting to add new constraints on this quantity.

4. Experimental set-up

G^0 experiment as other parity-violating experiments requires a high statistics (about 10^{13} elastic events) in order to measure very small asymmetries between 3 to 50 ppm with a relative error close to 5 %. This requires beam with high intensity

and high polarization. Also small helicity-correlated effects must come from the beam (intensity, position ...) and should be uncorrelated if possible to the detector and electronics response. The design of the experimental set-up has to achieve the highest possible rates with a long cryogenic target and a large acceptance of the detectors.

In the following we describe in more details all the items associated to the G^0 set-up from the beam properties to the magnet, target, detectors and electronics.

4.1. *Electron beam*

The polarized electrons are provided by the interaction of a circularly polarized laser on the strained GaAs photocathode, which allows to select a particular transition of the crystal. This method allows to achieve high polarization ($\geq 70\%$), which will be reversed at 30 Hz frequency (defining a macro-pulse period (MPS) of 33 ms) in less than 200 μs, by changing the polarity on a Pockels cell. In order to avoid time drift effects and to minimize the correlation of the helicity signal with the counting recording, the helicity will be randomly sequenced by quartet and will also be sent to the acquisition after a few MPS.

As previously mentionned, G^0 requires high intensity (40 μA) at a different mode than $CEBAF$ is usually operating (31 MHz instead of 500 MHz). This mode uses a charge per bunch 16 times larger than the normal operating, which implies new requirements on the beam optics, due to charge space effects [35]. The beam polarisation, will be measured with an accuracy of about 2 % using the standard Moller polarimeter available in hall C.

An important issue in this kind of experiment is related to the systematic errors associated to the beam properties. The resulting false asymmetries, induced by possible correlations between the counting rates in the detectors and the beam parameters (noted i) as the beam charge, positions, angles and energy, have to be corrected through the relation :

$$A_{corr} = A_{brut} + \sum_{i=1}^{i_{max}} \frac{1}{2N} \left(\frac{\delta N}{\delta P_i} \right) \Delta P_i \tag{19}$$

where ΔP_i is the difference on the beam parameters as a function of the helicity and $\left(\frac{\delta N}{\delta P_i}\right)$ corresponds to the detector response to the beam parameters. The way to minimize these systematic errors to an acceptable level is to keep ΔP_i as low as possible so the run-averaged correction on the asymmetry remains lower than the statistical error ($\simeq 10^{-7}$). Secondly, the beam parameter difference ΔP_i has to be measured accurately in such a way that the error on the correction (during the overall experiment) is kept as low as 5% ΔA_{stat} ($\simeq 5.10^{-9}$). Based on the results of the $HAPPEX$ experiment, these beam requirements, which are summarized from

each beam parameter on table 4, are achievable for the G^0 experiment.

Table 4. *Beam requirements for the G^0 functionning. These values are based on HAPPEX results achieved in 1999.*

Beam parameters	Nominal values	Beam fluctuation at 15 Hz	Helic. Corr. in 30 days
CW current	40 μA	0.2 %	$\leq$ 1 ppm
Energy	3 GeV	10^{-5}	$\leq 2.5 \times 10^{-8}$
Position	0 ± 0.2 mm	20 μm	$\leq$ 20 μm
Beam diam.	$\leq$ 200 μm	20 μm	$\leq$ 2 μm
Angle	0 ± 0.05 mrd	2 μrd	$\leq$ 2 nrd

4.2. *Target and spectrometer*

The G^0 experiment will use a 20 cm target which is axially symmetric (see figure 6). Its design, which is based on the one used in the $SAMPLE$ experiment, is optimized to reduce the energy loss on the scattered particles path, and to minimize density variations up to 250 W of beam power deposited in the target. Also the target can be removed from the beam trajectory for diagnostic purposes and can be warmed independently of the spectrometer. A manifold is used to direct the fluid flow down the center of the target cell and back near the cell walls. The target is fronted by a Helium cell which is used to extend the entrance of the hydrogen cell beyond the manifold so that exiting particles pass through only thin cell walls. It eliminates also variations in the target thickness with beam position.

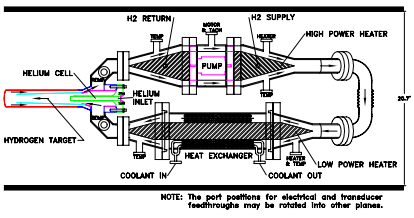

Figure 6. Design of G^0 target

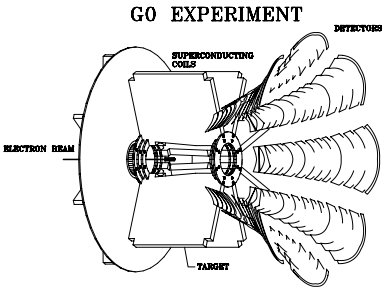

Figure 7. G^0 spectrometer .

The spectrometer is the master piece of the G^0 apparatus. It consists of a superconducting toroidal magnet with eight sectors placed around the beam axis

(see Fig. 7). The charged particles coming from the elastic scattering, produced in the target are selected in momentum by the magnetic field so that their location on the focal plane is independent from the interaction point along the beam axis. It has been designed to achieve large acceptance in solid angle (0.4-0.9 sr) which corresponds in the forward mode to a large Q^2 acceptance (0.1 to 1 $(GeV/c)^2$).

The high magnetic field (1.6 T.m. in the Forward mode) produces a bend angle of 35° which is associated to a collimator geometry allowing to remove the direct view from the target and thus reduce the background coming from neutral particles in the detectors. Horizontal collimators are installed in order to define accurately the azimuthal acceptance, which is about 22° for each octant, and prevent particles to be deviated in the neighbouring octants. Also vertical collimators are used to restrict the θ angular acceptance to the one corresponding to the elastic scattering and thus reduce counting rates from inelastic protons and pions.

4.3. *Forward angle measurement and the Focal Plane Detectors*

Detectors are located at the focal plane of the spectrometer for each of the eight octants defined by the coils. An octant is composed of 16 pairs of plastic scintillators coupled to light guides. The arc-shape of each scintillator has been calculated from simulated trajectories of elastic protons created along the target at fixed transfers momentum Q^2. As shown in figure 8, protons related to different Q^2 are scattered at a different location in the focal plane of the spectrometer and, for a fixed Q^2, all protons coming from different part of the target will be focused in the same detector.

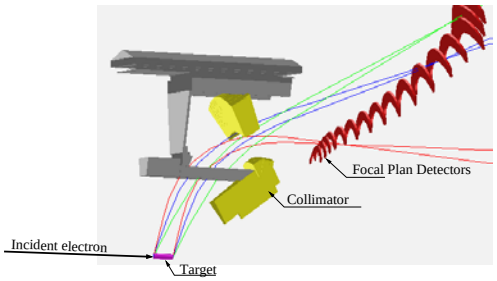

Figure 8. Trajectories of protons elastically scattered for three different Q^2=0.13, 0.25 and 0.7 $(GeV/c)^2$.

Figure 9. One octant with the 16 arc-shaped scintillators and light guides installed in the mechanical support.

The detector size have been optimized to limit the counting rates to 1-2 MHz. Also each detector is composed of a pair of scintillators separated by an aluminium

or plastic plate. The coincidence between these two active layers allows to reduce significantly the background related to neutral particles like neutrons and γ produced in the target and other materials. G^0 set-up has been simulated to provide counting rates of particles produced in elastic and inelastic reactions. Pions generators have been tested by comparing simulation with data obtained using the short orbit spectrometer (SOS) located in the hall C at the same kinematics than G^0 experiment [15]. Figure 10 shows the counting rates associated to each scintillator. As can be seen, the expected counting rates did not exceed 1.5 MHz and the scintillators size have been optimized to obtain a rather uniform counting in all detectors.

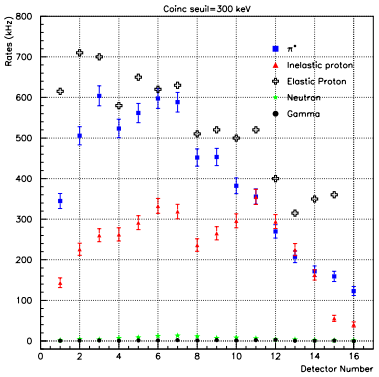

Figure 10. Simulated counting rates obtained for Front and Back coincidences.

Because PMTs must be located far away from the spectrometer in relatively low magnetic field regions, scintillators have been connected at each extremity to long light guides whose lengths range from 40 cm up to 2 m. Their design has been carefully studied in order to optimize the light collection at the PMT. Dedicated measurement have shown that several hundred photo-electrons will be available at the PMT level in the forward angle mode.

The elastic protons are discriminated from other particles (protons, pions etc ...) using time of flight measurement. Simulated time spectra (see figure 11) obtained for detectors 1 to 14 look very similar in shape with time difference between pions and elastic protons varying from 14 to 7 ns. Also inelastic protons can be separated from elastic protons (note the log scale). In order to optimize the experimental time resolution, the detectors are placed transverse to the particle trajectory in order to reduce spread on the time of flight. Also the choice of BC408 Bicron as scintillating material has been made to insure a good timing resolution (less than

0.5 ns) required for time measurement.

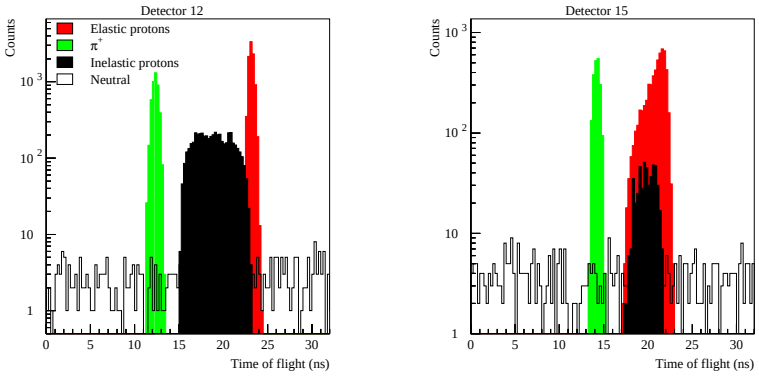

Figure 11. Simulated time of flight spectra associated to detectors 12 and 15.

Time spectrum associated to the detector 15, as shown in figure 11, is different compared to the other detectors because it is located at the maximum location allowed for elastic protons. Indeed higher momentum are associated to smaller scattering angle and will be located on detector 14 (but with different time of flight). Thus the large range in Q^2 in detector 15, from 0.5 to 1 $(GeV/c)^2$ is reflected in a wider time distribution associated to the elastic peak. Different binning in the time spectra will allow to define different Q^2 range.

One has to notice that the French and North-American parts of the collaboration have provided each four octants which differ only in details concerning light guides and mechanical support.

4.4. *Forward angle electronics*

For the forward angle measurement, the electronics needed for the asymmetry measurement has to provide time of flight information associated to each detector with rates ranging between 1 to 2 MHz. Also the electronics response has to be very stable through different experimental conditions to avoid any helicity correlated systematic effect. For example the electronics deadtime has to be minimized and known with a good accuracy.

Two different electronics, which will equip either four octants, have been built by the North-American and French parts of the collaboration. They should allow to study in detail different responses and related systematic effects. These two systems are based on the same concept, with the encoding of the time of flight associated to the Front scintillator, when requiring a coincidence with the Back detector. Then

the time information is histogrammed during one MPS and read out during the helicity reversal. As shown, in figure 12, the four analog signals, corresponding to the four PMTs of one detector, are sent into Constant Fraction discriminators (CFD). Time information associated to Left and Right PMTs are meantimed to cancel the time dependence versus the location of the interaction along the scintillator. Then the coincidence between the Front and the Back detectors is required to record the time of flight information. While the time range of 32 ns is fixed by the interval between two beam pulses, the time binning differs for the two electronics with 1 ns for the North-American and 250 ps for the French one.

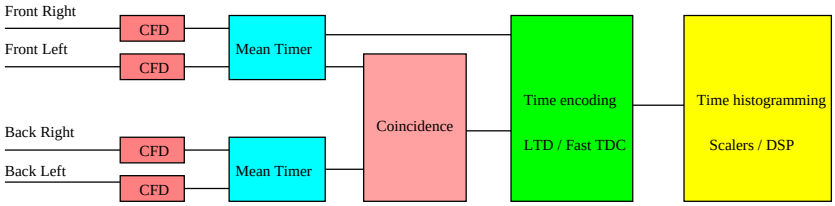

Figure 12. Schematic design of the forward angle electronics

The difference between the two electronics are mainly related to the principle of the time encoding and the time histogramming. The North-American electronics, is composed of several modules, with the time encoding system using shift registers clocked at 500 MHz (provided by the accelerator) and individual scalers used for the time histogramming. In the French integrated VXI module, the time encoding is obtained by a flash TDC synchronized on a 31.25 MHz and Digital Signal Processors (DSP), which provide the time histogramming [37].

Finally, the charge and time distributions associated to each discriminator and meantimer will also be prescaled from a standard event by event Fastbus acquisition and will be used to monitor possible drifts of gains and time resolution of PMTs. Fastbus acquisition is also used for recording information related to the beam.

5. Backward angle measurement, Cryostat Exit Detectors and Cerenkov counter

For the Backward angle measurement, electrons are detected at about 110° after the spectrometer, which will be turned relative to the beam direction. In this configuration the background is composed of electrons and negative pions coming from inelastic processes, which have the same velocity than the elastic electrons. Thus the time of flight cannot be used to discriminate between the different reactions and the selection between particles will be obtained from their different trajectories. Figure 13 shows some selected trajectories associated to elastic electrons. A

second hodoscope, composed of nine Cryostat Exit Detectors (CED), will allow to distinguish trajectories of elastic electrons from the others. These detectors which are located close to the spectrometer are connected to PMTs using long light guides (see figure 13).

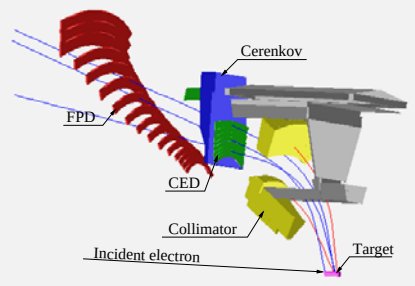

Figure 13. Elastic electrons trajectories at $Q^2 = 0.3\ (GeV/c)^2$.

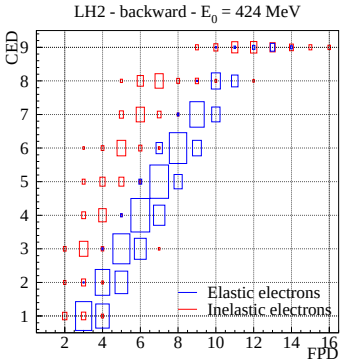

Figure 14. Coincidence matrix CED versus FPD at $Q^2 = 0.3(GeV/c)^2$. The squares size is proportional to the counting rates.

The associated counting rates have been simulated and plotted in figure 14 for the hydrogen target as a function of the numbering of the FPD and CED, which are fired. The same information will allow to measure at the same time the asymmetry measurement for electrons related to the Δ production at backward angle [13].

The π^- produced on deuterium target will not be completely rejected from the cuts applied to the CED-FPD coincidence matrix. Figure 15-Left shows that, at 0.8 $(GeV/c)^2$, the counting rates of pions produced in the deuterium target are dominating largely those of quasi-elastic electrons. Thus another particle identification is needed and will be provided by a Čerenkov counter. This trapezoidal-shaped detector, which is composed of 5 cm of aerogel with an 1.03 refractive index, produces Čerenkov light, which will enter in a light box covered with a diffuser and be detected by four 5-inches PMTs. It provides about 6 to 8 photo-electrons for quasi-elastic electrons, which will be shared over the four PMTs. It is almost insensible to pions up to 450 MeV/c, muons coming from pions desintegration and δ rays which are produced in several material located in front of the Čerenkov counter. A recent comparison between beam tests and simulation have shown [36], that a good electron efficiency of about 88 % and a pion rejection of about 140 (defined as the ratio between the electron and the pion efficiency) can be expected. Figure 15-Right shows

the expected counting rates after applying the particle identification in the worst case corresponding to the deuterium target at 0.8 $(GeV/c)^2$. The contamination is found to be low enough (note the log scale) to allow a good extraction of the asymmetry of the quasi-elastic scattering. The construction of the aerogel counter requires the extension of the mechanical support built for the forward angle mode. Also some caution has to be taken concerning the magnetic shielding associated to these PMTs and tests are under progress.

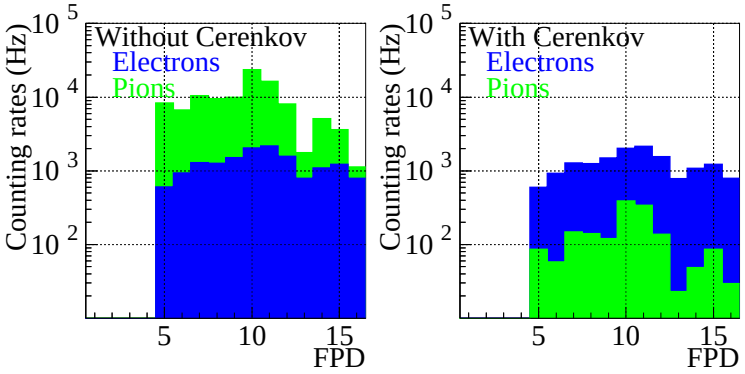

Figure 15. Counting rates associated to electrons and pions produced on deuterium target at 0.8 $(GeV/c)^2$ without (Left) and with (Right) the pion rejection given by the Čerenkov counter.

5.1. *Backward Angle Electronics*

Again the backward angle electronics is based on the requirement of high counting rates, although lower than in the forward angle mode, and on the need of coincidence recording. The electronics design makes use of part of the modules developped for the forward angle measurement and two different architecture will be installed on the French and North-American octants. The design, which is summarized on figure 16, is based on the coincidences counting between the CED and the FPD detectors. These coincidences will be performed during a short time window (about 8 ns) relative to the 32 ns between two beam pulse and will be enabled by the Cerenkov signal corresponding to the detection of electrons. Each of the 9×14 CED-FPD coincidence counting will then be histogrammed during the MPS and be transferred to the acquisition during the helicity reversal time. The CFDs and meantimers used for the Forward angle measurement will be used again. In the North-American design, the CED-FPD coincidence matrix, which is performed by a programmable ALTERA chip, is sent into the scalers already used in the forward mode. For the

French design, the VXI module built include the programmable ALTERA and all scalers. The Čerenkov signal is used to enable the scalers. Additional counting associated to individual counting including the Čerenkov validation (or not) and also counting associated to multi-hits configuration, where more than one (FPD or CED) detector is hitted, will be recorded using the programmable capability of the ALTERA. These information will be useful for further corrections associated to the deadtime losses and pile-up.

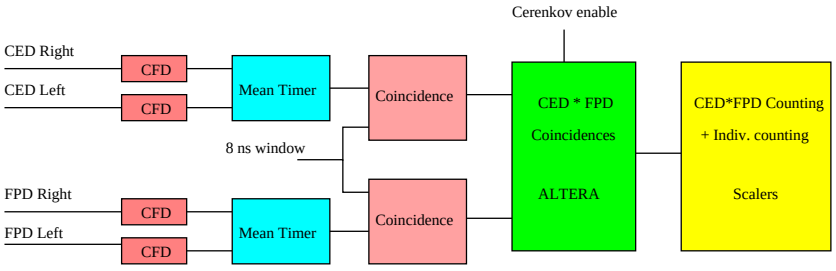

Figure 16. Shematic design of the backward angle electronics

5.2. *Summary*

The G^0 experiment represents the only opportunity in the next decade to measure independently the electric G_E^s, magnetic G_M^s and axial G_A^{ep} form factors for a wide range of momentum tranfers ($Q^2 = 0.3, 0.5$ and 0.8 $(GeV/c)^2$). These measurements will provide new information on the contribution of strange quarks to the nucleon structure and also allows a better understanding of the anapole term in the axial coupling of the photon to the nucleon.

For the G^0 experiment a completely new set-up has been designed. The experiment will perform its commissioning run between October 2002 and January 2003. Then the actual plan is to perform the forward angle measurement in one run of 700 hours between 0.1 to 1 $(GeV/c)^2$ at the end of 2003. Then after the turn-around of the spectrometer three different data taking with hydrogen and deuterium targets of 700 hours each are proposed by the G^0 collaboration corresponding to the three different Q^2 measurement. The data taking corresponding to the backward angle program could start in early 2005.

Acknowledgments

I would like to thank the organisers of PAVI2002 for their great hospitality. I would like also to thank all collaborators on G^0 experiment and wish successful incoming data taking. The G^0 experiment is supported by DOE (U.S.), CNRS/IN2P3 (France), NSERC (canada) and NSF (U.S.).

References

1. R. Vogt, Prog. in Part. and Nucl. Phys. **45** (2000) S105.
2. B.W. Filippone and X. Ji, Adv. in Nucl. Phys. **26** (2001) 1.
3. G.P. Ramsey *et al.*, hep-ph/0201041 (2002); G.P. Ramsey, Prog. in Part. and Nucl. Phys. **B39** (1997) 599.
4. J. Glasser, H. Leutwyler and M. Sainio, Phys. Lett. **B253** (1994) 252; T.W. Donnelly, Nucl. Phys. **A623** (1997) 223c.
5. D. Kaplan and A. Manohar, Nucl. Phys. **B310** (1988) 527.
6. R.D. McKeown, Phys. Lett. **B219** (1989) 140.
7. D.H. Beck, Phys. Rev. **D39** (1989) 3248.
8. M. Musolf *et al.*, Phys. Rep. **239** (1994) 1; T.W. Donnelly, Nucl. Phys. **A623** (1997) 223c.
9. D.H. Beck and B. Holstein, Int. Jour. Mod. Phys. **E10** (2001) 1.
10. D.H. Beck and R.D. McKeown, Ann. Rev. Part. Sci. **51** (2001) 189.
11. K.S. Kumar and P.A. Souder, Prog. in Part. and Nucl. Phys. **45** (2000) S33; K.S. Kumar, in these proceedings.
12. R.D. McKeown and M.J. Ramsey-Musolf, hep-ph/0203011 v1 (March 2002).
13. S. Wells, these proceedings; S. Wells *et al.*, Jefferson Lab Proposal E97-104.
14. T.W. Donnelly, Modern Topics in Electron Scattering, World Scientific Publishing (B. Frois and I. Sick Editors), ISBN 9971-50-975-X, 1991, p. 566; T.W. Donnelly and A.S. Raskin, Ann. Phys. **169** (1986) 247.
15. R. Tieulent, Ph.D. thesis, Grenoble University ISN 02-27 (2002).
16. L. Diaconescu, R. Schiavilla and U. van Kolck, Phys. Rev. C **63** (2001)044007.
17. E. Hadjimichael, G.I. Poulis and T.W. Donnelly, Phys. Rev. **C45** (1992) 2666.
18. M. Musolf and M. Burkardt, Z. Phys. **C61** (1994) 433.
19. W. Koepf *et al.*, Phys. Lett. **B288** 11 (1992); W. Koepf and E. Henley, Phys. Rev. **C59** (1994) 2219.
20. P. Mergell *et al.*, Nucl. Phys. **A596** (1996) 367.
21. H. Forkel, Phys. Rev. **C56** (1996) 510.
22. S. Dong *et al.*, Phys. Rev. **D58** (1998) 074504.
23. M. Ramsey-Musolf and H. Ito, Phys. Rev. **C55** (1997) 3066.
24. M. Musolf *et al.*, Phys. Rev. **D55** (1997) 2741.
25. X. Ji and J. Tang, Phys. Rev. **B362** (1995) 182.
26. W.M. Alberico *et al.*, Phys. Rep. **358** (2002) 227.
27. S. Zhu *et al.*, Phys. Rev. **D62** (2000) 033008.
28. C. M. Maekawa, J. S. Veiga and U. van Kolck, Phys. Lett. **B488** (2000) 167.
29. K.A. Aniol *et al.*, Phys. Lett. **B509** (2001) 211.
30. D. Spayde *et al.*, Phys. Rev. Lett. **84** (2000) 1106.
31. R. Hasty *et al.*, Science 290 (2000) 2117.

32. D. Spayde *et al.*, in these proceedings.
33. F. Maas *et al.*, in these proceedings.
34. Jefferson Lab Proposal E99-115; Jefferson Lab Proposal E00-114; D. Lhuillier *et al.*, these proceeding.
35. J. Crame *et al.*, in these proceedings.
36. J. Martin *et al.*, in these proceedings.
37. D. Marchand *et al.*, in these proceedings.